Structural and magnetic properties of betaine adducts with transition metals: I. $((CH_3)_3NCH_2COO)_3MnMCl_4$ with M = Mn^{2+}, Co^{2+}, Zn^{2+}

2006 J. Phys.: Condens. Matter 18 11067

(http://iopscience.iop.org/0953-8984/18/49/002)

INSTITUTE OF PHYSICS PUBLISHING JOURNAL OF PHYSICS: CONDENSED MATTER

J. Phys.: Condens. Matter **18** (2006) 11067–11079 doi:10.1088/0953-8984/18/49/002

Structural and magnetic properties of betaine adducts with transition metals: I. $((CH_3)_3NCH_2COO)_3MnMCl_4$ with M = Mn^{2+}, Co^{2+}, Zn^{2+}

Leonore Wiehl[1,4], Jürgen Schreuer[1], Eiken Haussühl[1], Björn Winkler[1], Katarina Removic-Langer[2], Bernd Wolf[2], Michael Lang[2] and Victor Milman[3]

[1] Johann Wolfgang Goethe-Universität Frankfurt, FOR 412, Institut für Geowissenschaften, Senckenberganlage 30, D-60054 Frankfurt am Main, Germany
[2] Johann Wolfgang Goethe-Universität Frankfurt, FOR 412, Physikalisches Institut, Max-von-Laue-Straße 1, D-60438 Frankfurt am Main, Germany
[3] Accelrys Inc, 334 Science Park, Cambridge CB4 0WN, UK

E-mail: L.Wiehl@kristall.uni-frankfurt.de

Received 28 July 2006, in final form 23 October 2006
Published 22 November 2006
Online at stacks.iop.org/JPhysCM/18/11067

Abstract

Large single crystals with diameters up to 20 mm of betaine adducts with 3d metals, namely $3b{\cdot}MnCl_2{\cdot}MCl_2$ with M = Mn^{2+} (BMM), Co^{2+} (BMC) and Zn^{2+} (BMZ), were grown from aqueous solution by slow evaporation of the solvent. The isomorphous crystal structures, space group $P\bar{3}$, are built up from carboxylate-bridged octahedral chains and isolated MCl_4 tetrahedra. The magnetic susceptibilities of these low-dimensional spin-systems were determined by superconducting quantum interference device (SQUID) measurements and are interpreted with an antiferromagnetic Heisenberg-chain model. We studied by experiment and density functional theory (DFT) calculations how the replacement of half of the Mn content ($S = 5/2$) in $3b{\cdot}2MnCl_2$ by metals with different spin (Co, $S = 3/2$; Zn, $S = 0$) modifies the structural and magnetic properties. The results show that, predominantly, Mn occupies the octahedral sites in the chains and is responsible for the magnetic interaction, whereas the other metal (Co or Zn) is found on the isolated tetrahedral sites.

(Some figures in this article are in colour only in the electronic version)

1. Introduction

Since the discovery of the antiferroelectric phase transition in betaine phosphate [1], adducts of betaine, b = $(CH_3)_3NCH_2COO$, with inorganic and organic acids as well as with metal salts,

[4] Author to whom any correspondence should be addressed.

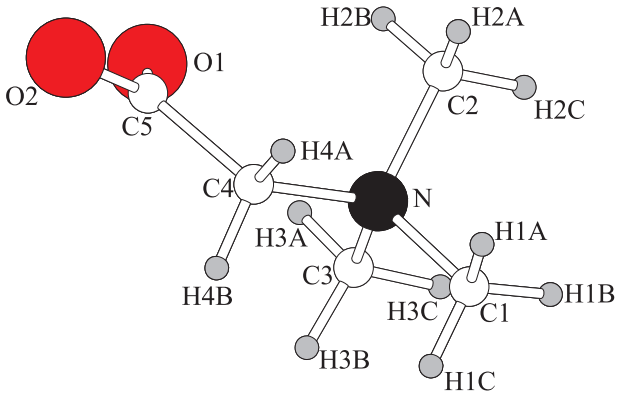

Figure 1. The betaine molecule with atomic labelling as used in this work.

have attracted much attention. Particularly remarkable is the rich variety of phase transitions of which the incomplete devil's staircase observed in betaine calcium chloride dihydrate, b·$CaCl_2$·$2H_2O$, is the most outstanding example [2, 3]. Recently, betaine compounds have been considered a potential source of crystal species possessing low-dimensional magnetic structures [4]. Due to its delocalized π-system the carboxylate group on one end of the betaine molecule (figure 1) can act as a bridging ligand providing a super-exchange pathway between spin-bearing metal ions. The large trimethylammonio part on the other end behaves like a spacer that can separate adjacent chains of magnetic ions. One-dimensional arrangements of cation polyhedra have been reported, for example, for 2b·$Cu(NO_3)_2$·$Cu(N_3)_2$ [5] and for certain adducts of betaine with $MnCl_2$ [6–8] and cadmium salts [9].

In the course of a systematic search for new crystal species possessing low-dimensional spin-systems, we recently reported the crystal structures of two new adducts of betaine with manganese(II) and cobalt(II) or zinc(II) chloride, namely 3b·$MnCl_2$·$CoCl_2$ (BMC) and 3b·$MnCl_2$·$ZnCl_2$ (BMZ) [10]. They are isomorphous to 3b·$2MnCl_2$ (BMM) [6, 7], which crystallizes in the trigonal space group $P\bar{3}$. All three compounds are built up from polymeric chains of MnO_6 octahedra, which are connected via the carboxylate groups of the betaine molecules (figure 2). Within these chains, magnetic interactions between the Mn^{2+} cations (spin 5/2) are expected. The other metal ions (M = Mn^{2+} (spin 5/2), Co^{2+} (spin 3/2), and Zn^{2+} (spin 0)) occupy slightly distorted tetrahedral MCl_4 sites. They are located on threefold axes in between the chains, filling the holes between the methylammonium groups of the betaine molecules.

In order to study the magnetic interactions within the octahedral chains, we measured the magnetic susceptibilities of 3b·$MnCl_2$·MCl_2 with M = Mn^{2+}, Co^{2+} and Zn^{2+} using the SQUID technique. Additionally, we performed calculations based on density functional theory (DFT) to understand the influence of different occupations of cation sites on structural and physical properties.

2. Experimental details

2.1. Crystal synthesis

The title compounds were synthesized by dissolving in pure water stoichiometric quantities of betaine monohydrate ($C_5H_{11}NO_2$·H_2O) and of the corresponding metal(II) chlorides $MnCl_2$, $CoCl_2$·$6H_2O$ and $ZnCl_2$, respectively.

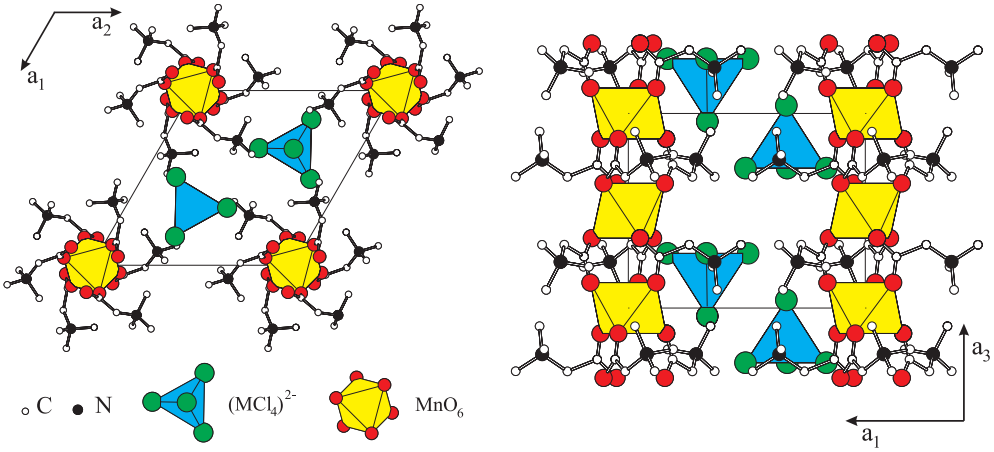

Figure 2. Projections of the unit cell of trigonal 2b·$MnMCl_4$ on the (001) plane (left) and (010) plane (right) in trigonal–hexagonal setting. The principal bond chains parallel to the threefold axis consist of carboxylate-bridged MnO_6 octahedra.

The crystal growth experiments were performed using air thermostats, each providing space for two glass vessels containing up to 10 l of solution. The temperature range inside the thermostats can be set between 260 and 330 K. The required oversaturation is achieved in the well stirred solution by controlled lowering of temperature (typically 0.05 K/day) or by slow evaporation of the solvent. The temperature stability provided by a PID controller is ± 0.02 K. To maintain temperature stability near or even below room temperature, we employ a secondary chiller system with a large external cooling reservoir. An automatic temperature adaptation ensures a sufficient temperature difference between cooling reservoir and growth vessel.

Large single crystals of BMM and BMZ of diameters up to 20 mm were grown within four weeks by slow evaporation of the solvent at ambient temperature. Working with growth rates of about 0.5 mm/day, single crystals of optical quality (BMM) could be obtained. Small crystals of 3 mm in diameter, obtained by evaporation at ambient conditions, were used as seed crystals. Crystals of BMZ show a pale pink colour, whereas BMM is light yellow. The morphology of both crystal species is dominated by the hexagonal prism {100} and the pinakoid {001}. Good cleavage is observed parallel to the prism faces.

In the case of BMC, only elongated prismatic crystals of up to 3 mm in length with an aspect ratio of about 2 were obtained. The dark blue crystals possess the same morphology as BMM and BMZ. Progress of crystal growth is difficult to control because of the high viscosity and the opacity of the saturated aqueous solution of BMC.

The crystal structures of BMZ and BMC [10] were determined by single-crystal X-ray diffraction, using an Xcalibur3 four-circle diffractometer from Oxford Diffraction with a CCD camera and a sealed tube with Mo Kα radiation. Lattice parameters of the title compounds as determined by single-crystal X-ray diffraction techniques are given in table 1. Selections of relevant bond distances and angles are listed in tables 2 and 3.

2.2. Magnetic measurements

Magnetic measurements were performed in the temperature range between 2 and 300 K and fields up to 5 T with a Quantum Design MPMS SQUID system. The uncertainty of the

Table 1. Experimental and theoretical lattice parameters and densities ρ calculated from unit-cell volume and chemical composition of 3b·2$MnCl_2$ (BMM), 3b·$MnCl_2$·$CoCl_2$ (BMC) and 3b·$MnCl_2$·$ZnCl_2$ (BMZ). These isostructural compounds crystallize in space group $P\bar{3}$. In the case of BMZ the parameters were calculated for ferromagnetic (FM) and antiferromagnetic (AFM) spin ordering within the chain.

Compound	Reference	a (Å)	c (Å)	V (Å^3)	ρ (g cm^{-3})
BMM	[6]	12.880(2)	9.117(1)	1309.9	1.529
BMM	[7]	12.881(3)	9.107(4)	1308.6	1.531
BMM	(Exp., this work)	12.865(2)	9.093(1)	1303.3	1.537
BMM	(DFT, this work)	13.46	9.124	1431	1.400
BMC	[10]	12.783(1)	9.077(1)	1284.5	1.570
BMZ	[10]	12.775(1)	9.084(1)	1283.8	1.587
BMZ (FM)	(DFT, this work)	13.434	9.086	1420	1.437
BMZ (AFM)	(DFT, this work)	13.426	9.092	1420	1.437

Table 2. Selected experimental bond distances d_e, calculated bond distances d_c and bond populations p_c of BMM and BMZ. For comparison, the experimental values of BMC are included.

	BMM			BMZ			BMC
	Exp.	DFT-GGA		Exp.	DFT-GGA		Exp.
	d_e (Å)	d_c (Å)	p_c [e^-]	d_e (Å)	d_c (Å)	p_c [e^-]	d_e (Å)
Mn1–O1	2.184(1)	2.235	0.19	2.182(1)	2.230	0.19	2.182(1)
Mn2–O2	2.158(1)	2.185	0.21	2.159(1)	2.190	0.21	2.158(1)
M3–Cl2	2.364(1)	2.368	0.36	2.270(1)	2.290	0.41	2.281(1)
M3–Cl1	2.369(1)	2.410	0.32	2.285(1)	2.330	0.36	2.283(1)
O1–C5	1.246(2)	1.266	0.94	1.248(2)	1.266	0.95	1.242(2)
O2–C5	1.252(2)	1.274	0.93	1.253(2)	1.274	0.93	1.253(2)
C4–C5	1.523(3)	1.532	0.71	1.522(3)	1.533	0.72	1.525(3)
N–C4	1.501(3)	1.515	0.56	1.503(2)	1.516	0.57	1.503(3)
N–C3	1.493(3)	1.503	0.55	1.491(3)	1.504	0.56	1.493(3)
N–C2	1.491(4)	1.503	0.56	1.493(3)	1.502	0.56	1.496(3)
N–C1	1.497(3)	1.504	0.56	1.497(3)	1.504	0.57	1.497(3)
C1–H1A	0.98(4)	1.096	0.84	0.97(4)	1.097	0.86	1.03(4)
C1–H1B	0.95(4)	1.096	0.84	0.98(3)	1.096	0.85	1.02(3)
C1–H1C	0.90(4)	1.097	0.84	0.91(3)	1.097	0.85	0.89(3)
C2–H2A	0.94(5)	1.094	0.85	0.98(4)	1.094	0.85	0.97(4)
C2–H2B	0.94(4)	1.092	0.87	0.93(4)	1.092	0.87	0.90(3)
C2–H2C	0.93(3)	1.096	0.85	0.97(3)	1.097	0.86	0.99(3)
C3–H3A	0.89(4)	1.092	0.85	0.93(4)	1.091	0.86	0.87(3)
C3–H3B	0.96(4)	1.096	0.86	0.96(3)	1.096	0.87	0.96(4)
C3–H3C	1.02(4)	1.097	0.86	1.00(3)	1.097	0.88	1.02(3)
C4–H4A	0.96(3)	1.097	0.89	0.95(3)	1.098	0.89	0.96(3)
C4–H4B	0.92(3)	1.101	0.85	0.94(3)	1.101	0.86	0.95(3)

temperature is less than 0.01 K at low temperatures and the resolution of the magnetic moments is in the order of 1×10^{-7} emu. For temperatures below 2.5 K and down to 0.1 K the magnetic susceptibility was determined with an ac technique adapted to a ^{3}He/^{4}He dilution refrigerator. Here the temperature can be determined to ± 0.005 K whereas the resolution of the susceptibility is reduced by a factor of ten in comparison with the SQUID. Single crystals of

Table 3. Selected bond angles from X-ray diffraction. (Note: Equivalent positions: (i) $-y, x-y, z$, (ii) $-x+y, -x, z$, (iii) $-x, -y, -z$ and (iv) $x-y, x, -z$.)

	BMM angle (deg.)	BMZ angle (deg.)	BMC angle (deg.)
O1–Mn1–O1^{iii}	180	180	180
O1–Mn1–O1^{ii}	93.16(5)	93.20(5)	93.18(5)
O1–Mn1–O1^{iv}	86.84(5)	86.80(5)	86.82(5)
O2–Mn2–O2^{iii}	180	180	180
O2–Mn2–O2^{iv}	91.77(6)	91.52(5)	91.55(5)
O2–Mn2–O2^{ii}	88.24(6)	88.48(5)	88.45(5)
Cl2–M3–Cl2^{i}	112.88(2)	112.37(2)	112.27(2)
Cl2–M3–Cl1	105.80(3)	106.38(2)	106.50(3)

BMZ, BMM and BMC with masses of 35.0 mg (BMZ), 65.0 mg (BMM) and 44.7 mg (BMC) were used for the experiments. The rectangular parallelepipedal sample of BMM with edge lengths of about 3 mm and edges parallel and perpendicular to the threefold axis were cut from a large single crystal using a wire saw built in house. Opposite faces of the sample were parallel to within ± 5 μm. The orientation of the sample was controlled by Laue diffraction. All susceptibility data were corrected for a temperature-independent diamagnetic contribution according to Kahn [11].

3. Computational details

Our quantum mechanical calculations are based on density functional theory, DFT. While DFT itself is exact [12], actual calculations require an approximation for the treatment of the exchange and correlation energies. Here we use the 'generalized gradient approximation', GGA [13]. Results based on GGA calculations are generally in better agreement with experiment than those obtained with the local density approximation, LDA [14–17].

The unit-cell volumes of BMM, BMC and BMZ are about 1400 Å^3, and there are 126 atoms per unit cell, which requires a computationally efficient approach. Computational schemes in which the charge density and electronic wavefunctions are expanded in a basis set of plane waves are well established for structures of such complexity. However, as it is impractical to consider tightly bound core electrons explicitly when using a plane-wave basis set, pseudopotentials have to be used to mimic the screening of the Coulomb potential of the nucleus by the core electrons. A number of approaches for the construction of pseudopotentials have been presented in the literature [18, 19]. The state of the art are the efficient 'ultra-soft' pseudopotentials, which require a comparatively small number of plane waves [20, 21]. Such ultra-soft pseudopotentials were used here, with a maximum cut-off energy of the plane waves of 380 eV. In addition to the cut-off energy, only one further parameter determines the quality of the calculations, namely the density of points with which the Brillouin zone is sampled. We used a Monkhorst–Pack grid, in which the distances between grid points were ≈ 0.05 Å^{-1}. This is a rather strict criterion for obtaining ground state properties of an insulator. Spin-polarized calculations were performed. For BMZ, we started calculations with both an antiferromagnetic spin arrangement and a ferromagnetic one, using formal spins. In all calculations, the total spin was allowed to vary. After the final self-consistency cycle, the remaining forces on the atoms were less than 0.04 eV Å^{-1}, and the remaining stress was less than 0.03 GPa, while no component of the stress tensor was larger than 0.04 GPa. The present calculations are restricted

to the athermal limit, in which temperature effects and zero-point motions are neglected. For the calculations we used academic and commercial versions of the CASTEP program, which has been described elsewhere [22–24].

In addition to the title compounds we computed the structure of a hypothetical anti-ordered BMZ polymorph, in which all Zn atoms are octahedrally coordinated while the Mn are in fourfold coordination. The computational details were identical to those employed for the inversely ordered polymorph.

4. Results and discussion

4.1. Crystal structure

Single-crystal X-ray structure determinations [6, 7, 10] revealed chains of carboxylate-linked $M^{2+}O_6$ octahedra along [001] (figure 2) as the characteristic structural feature of the title compounds. Charge compensation is provided by isolated $[MCl_4]^{2-}$ groups (distorted tetrahedra) between the chains. The chains are surrounded by voluminous trimethylammonio tails of the betaine molecules, which are involved only in weak van der Waals contacts with their neighbours. The delocalized π-electron systems of the carboxylate bridges in combination with the metal–metal distances of about 4.5 Å enable magnetic interactions of the cations within the chains. However, the metal ions in the tetrahedral positions are too far separated from each other, and from the chains, to participate in magnetic interactions. In BMM, for example (Mn1, Mn2 in chain, Mn3 in tetrahedra), the respective distances are d(Mn1–Mn3) = 7.68 Å, d(Mn2–Mn3) = 7.89 Å and d(Mn3–Mn3) = 8.36 and 9.12 Å. In BMC and BMZ the corresponding distances differ by less than 1%.

Whereas in BMM the octahedral and tetrahedral lattice sites are both occupied by manganese, the cation distribution in BMZ and BMC is not obvious. Crystal chemical experience suggests that Zn prefers a tetrahedral coordination. Thus for BMZ the experimentally observed type of occupation [10] was expected. A possible mixing of Mn and Zn on the octahedral and tetrahedral lattice sites was tested by refining partial site occupation factors in the final states of structure calculations. For both of the inequivalent octahedral Mn sites, a partial occupation of Zn was tested. Similarly, a partial occupation of Mn on the tetrahedral Zn site was tested. In both cases these occupation factors refined to values of zero within the statistical error. This is compatible with the results of magnetic measurements, which show an amount of about 0.4% uncoupled Mn^{2+} $S = 5/2$ spins.

For BMC, on the other hand, the situation is unclear, because in X-ray diffraction the difference of atomic scattering factors between Mn and Co is significantly smaller than for the pair Mn–Zn. Refinements of partial site occupation factors were unstable or yielded unreasonable atomic displacement parameters (ADPs) due to high correlations between the free parameters. However, structure calculations for several sets of fixed partial site occupation factors resulted in nearly unchanged residuals and only slightly altered ADPs as long as the amount of manganese on the Co site or cobalt on a Mn site did not exceed 20%. Larger amounts of Mn–Co disorder worsened the results considerably.

Many examples of octahedral and tetrahedral Co^{2+} complexes [25] show that there are no pronounced chemical preferences. The deep blue colour of the BMC crystals hints at a predominantly tetrahedral coordination, as this colour is characteristic for many compounds containing $CoCl_4$ or CoO_4 tetrahedra, whereas e.g. the octahedral $[Co(H_2O)_6]^{2+}$ complex is coloured pink. Moreover, the possible replacement of Mn by Co in the octahedral chain is clearly limited. Neither $3b{\cdot}CoCl_2{\cdot}ZnCl_2$ nor $3b{\cdot}2CoCl_2$ exist; in the respective solutions, we found that only phases of different composition and symmetry grew.

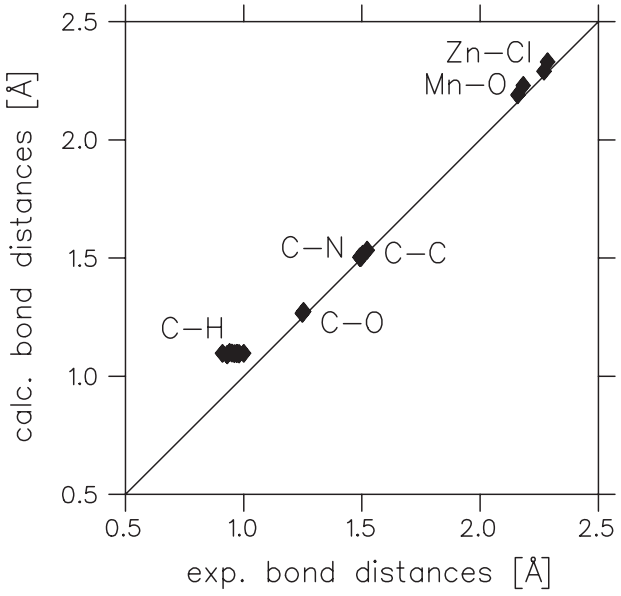

Figure 3. Comparison of experimental (X-ray diffraction) and calculated (DFT-GGA) bond distances of BMZ. BMM and BMC give comparable results.

4.2. Modelling of crystal structures with DFT calculations

For BMZ, the DFT calculations yielded lattice parameters of $a = 13.434$ Å and $c = 9.086$ Å, i.e. a unit-cell volume of 1420 $Å^3$. While the experimental and theoretical values for the c-lattice parameter are in very good agreement, the overestimation of the a-lattice parameter by 5% is larger than that usually observed in calculations such as those employed here, where the typical 'GGA under-binding' generally leads to an overestimation of not more than 3%. However, the chains running parallel to the c-axis are not linked by covalent bonds within the a, b-plane. Van der Waals interactions are only poorly described by DFT-GGA calculations, and purely van der Waals bound structures are often not even stable. However, for the following discussion, this comparatively large discrepancy between theory and experiment is irrelevant, as it concerns only directions perpendicular to the chains.

The results of the geometry optimization for the bond distances are compared to experimental data in table 2 and in figure 3. Clearly, the calculations give a satisfactory description of the structure within the expected accuracy of DFT calculations such as those employed here. Generally, it can be expected that interatomic distances are reproduced or predicted to within 0.03–0.07 Å [23], and this is what has been observed here. The only significant differences are between the experimental and the theoretical C–H distances. The theoretical values vary within 0.005 Å about a value of 1.096 Å for all C–H bonds, and are certainly more reliable than those obtained from the X-ray structure refinement [26].

The enthalpies of the ferromagnetic and antiferromagnetic structures were equal to within 0.04 eV per unit cell. This small difference is insignificant, as it will be due to the very small differences in the final stress tensor and the final resultant forces acting on the atoms. The projection of the spin density on a minimal localized basis set resulted in a charge of 1.41 and $1.29e^-$ for the two symmetrically independent Mn atoms. The corresponding spins (in units of $\hbar$) were 2.34 and 2.39 in the ferromagnetic case and 2.33 and −2.38 in the antiferromagnetic

case. Hence, the Mn are always in a high-spin configuration, which formally would correspond to five unpaired electrons per Mn^{2+}. The Zn has a charge of $1.24e^-$. The charges associated with the carbon atoms vary between -0.4 and $-0.6e^-$, with the notable exception of the carbon atom C5 of the carboxylate group. C5 has a significant positive charge of $0.6e^-$.

The quantum mechanical calculations show that it is energetically very unfavourable to incorporate Zn into the octahedral sites in BMZ. In the most simple mean field approximation, where the energy difference is given as a function of the probability of atom A occupying site α, and atom B occupying site β, or vice versa, i.e.

$$E = P_{A_\alpha} E_{A_\alpha} + P_{B_\alpha} E_{B_\alpha} + P_{A_\beta} E_{A_\beta} + P_{B_\beta} E_{B_\beta} \tag{1}$$

the probabilities are related to an order parameter Q so that

$$P_{A_\alpha} = P_{B_\beta} = 0.5(1 + Q) \tag{2}$$

$$P_{B_\alpha} = P_{A_\beta} = 0.5(1 - Q). \tag{3}$$

The energy is then given as

$$E = 0.5(E_{A_\alpha} + E_{B_\alpha} + E_{A_\beta} + E_{B_\beta} + QE_{A_\alpha} - QE_{A_\beta} + QE_{B_\beta} - QE_{B_\alpha}) \tag{4}$$

$$= \text{const.} + 0.5Q(E_{A_\alpha} + E_{B_\beta} - E_{A_\beta} - E_{B_\alpha}) \tag{5}$$

$$= \text{const.} + \tfrac{1}{2} Q \Delta E. \tag{6}$$

The free energy is $F = E - TS$, where the entropy $S = -2R(0.5(1 + Q)\ln(0.5(1 + Q)) + 0.5(1 - Q)\ln(0.5(1 - Q)))$, so that

$$F = \frac{1}{2}\Delta E Q + T R \left((1 + Q) \ln \left(\frac{1 + Q}{2} \right) + (1 - Q) \ln \left(\frac{1 - Q}{2} \right) \right). \tag{7}$$

The site occupation can then be obtained from

$$Q = \frac{\exp(A) - 1}{\exp(A) + 1} \tag{8}$$

with $E = -40$ kJ mol^{-1} and $A = 0.5E/RT$. An assumed equilibrium temperature of 320 K then leads to 0.1% Zn in octahedral coordination. This first order estimate therefore is consistent with the interpretation of the magnetization curves and the constraints imposed by the crystal structure refinement.

The calculation of the anti-ordered BMZ structure, in which Zn is octahedrally coordinated, while the Mn are located in the tetrahedra, yielded lattice parameters which differed significantly from the ordered structure as shown in figure 4. The a-axis was lengthened by 0.05 to 13.485 Å, while the c-axis was shortened by 0.129 to 8.957 Å. This leads to an overall volume reduction by 10 to 1410.70 Å^3. The enthalpy of this hypothetical anti-ordered structure is 0.83 eV per unit cell less stable than the ordered polymorph. This corresponds to an energy difference of 40 kJ mol^{-1} per Mn–Zn pair. The Mn ions have a charge of $0.88e^-$, and are in the high-spin state (each having a spin of $2.34\hbar$), while the charges of the two symmetrically independent Zn are 1.71 and $1.66e^-$, respectively.

The calculations for BMM gave very similar results to those obtained for BMZ (tables 2 and 3 and figure 4). There are only very small changes in those parts of the structure which are comparable, i.e. the betaine fragment and the octahedrally coordinated Mn. Specifically, the spin and charge of the octahedrally coordinated Mn is the same within the accuracy of the calculations. In BMM, we can compare the two differently coordinated Mn atoms. In comparison to the octahedrally coordinated Mn, the tetrahedrally coordinated Mn has a very different charge of $0.91e^-$ (in comparison to 1.42 and $1.30e^-$ for the octahedrally coordinated Mn), but also has a high-spin configuration (spin of $2.34\hbar$). Hence, according to

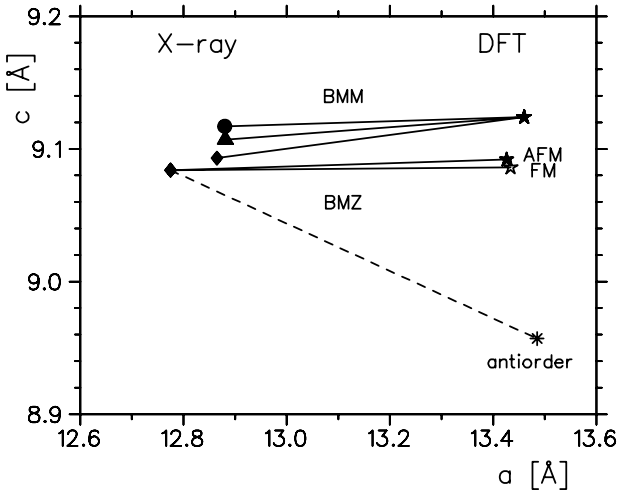

Figure 4. Lattice parameters c versus a for BMM and BMZ from X-ray diffraction (cf table 1) and DFT calculations.

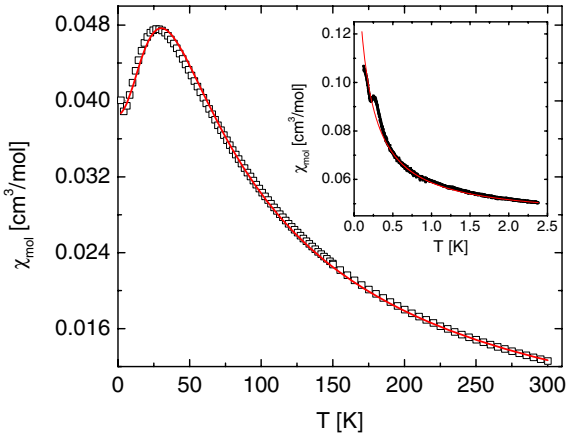

Figure 5. Molar magnetic susceptibility χ_{mol} of 3b·$MnCl_2$·$ZnCl_2$ (BMZ) in a field of $B = 0.5$ T applied parallel to the c-axis. The solid line is a fit to the experimental data based on a model for an antiferromagnetic Heisenberg spin chain (see the text for details). Inset: low-temperature data of χ_{mol} together with a Curie–Weiss fit, which accounts for uncoupled Mn^{2+} $S = 5/2$ spins.

our calculations, BMM has a distinct mixed valence character. The experimental ionic radius of tetrahedrally coordinated Mn^{2+} is 0.66 Å, while that for Zn^{2+} is 0.60 Å [27]. On exchange of Zn by Mn, we compute an increase of the two symmetrically independent M–Cl distances by about 0.08 Å, in excellent agreement with experiment.

4.3. Interpretation of magnetic measurements

Figure 5 exhibits the temperature dependence of the molar magnetic susceptibility χ_{mol} measured on a single crystal of 3b·$MnCl_2$·$ZnCl_2$ (BMZ). The data have been taken in a magnetic field of 0.5 T applied parallel to the c-axis (along the polymeric chains of the MnO_6 octahedra). A temperature-independent diamagnetism due to core contributions according to

Kahn [11] has been subtracted from the data. The analysis of the low-temperature susceptibility in the temperature range between 0.1 and 2.5 K, shown in the inset of figure 5, results in a small concentration of uncoupled $S = 5/2$ spins of 0.4%. The corresponding paramagnetic Curie contribution, which dominates the low-temperature part of $\chi_{\mathrm{mol}}(T)$, has also been subtracted from the data shown in the main panel of figure 5. With decreasing temperature $\chi_{\mathrm{mol}}(T)$ shows a Curie–Weiss-like increase followed by a pronounced maximum around 28 K. An extrapolation of the low-temperature data to $T = 0$ K yields $\chi_{\mathrm{mol}} = 0.0385$ cm^3 mol^{-1}.

The molar susceptibility of BMZ displayed in figure 5 is typical for a low-dimensional spin system governed by short-range spin correlations. From the high-temperature part, which can be well described by a Curie–Weiss susceptibility with $S = 5/2$, a g-factor $g = 2$ and an antiferromagnetic Weiss temperature $\Theta_{\mathrm{W}} = -42.5$ K, an average antiferromagnetic interaction between neighbouring Mn^{2+} spins is inferred. For a quantitative discussion of the susceptibility we thus model the system to be composed of independent antiferromagnetic Heisenberg chains, consistent with the crystal structure. The corresponding Hamiltonian is given by:

$$H = -2J \sum_{i=1}^{\infty} \vec{S}_i * \vec{S}_{i+1}. \tag{9}$$

By fitting the data shown in figure 5 with the expression given by Hiller [28], employing the intra-chain magnetic exchange coupling constant J between Mn^{2+} ($S = 5/2$) ions and their concentration c as free parameters, a reasonable description (cf. solid line in figure 5) is achieved with $J/k_{\mathrm{B}} = -(3.0 \pm 0.15)$ K and a concentration $c = 99.76\%$ of Mn^{2+} ions in the chain. This value of J is consistent with the Weiss temperature of $\Theta_{\mathrm{W}} = -42.5$ K. In a mean field approach where only the nearest neighbours z are taken into account, $\Theta_{\mathrm{W}} = 2z(S(S+1))J/3k_{\mathrm{B}}$, one obtains $\Theta_{\mathrm{W}} = -35$ K for BMZ [29]. As possible sources of inaccuracy in our fitting procedure, we mention (i) the presence of magnetic impurities with spin states different from $S = 5/2$, (ii) finite inter-chain interactions and (iii) local magnetic anisotropies. Since the inclusion of any of these effects would introduce several additional fitting parameters, we refrain from considering them here.

The inset of figure 5 shows the susceptibility for temperatures 0.12 K $< T <$ 2.4 K measured with an ac susceptometer adapted to a ^{3}He–^{4}He dilution refrigerator. For temperatures down to about 0.4 K the data nicely follow a Curie–Weiss-like temperature dependence (solid line). For lower temperatures, however, the susceptibility increases faster than expected from the Curie–Weiss fit and reveals a peak anomaly at 0.25 K. Since the susceptibility of uncoupled Heisenberg spin chains is constant (apart from small logarithmic corrections) in this temperature range, we assume that this anomaly is due to a long-range antiferromagnetic order as a result of a weak inter-chain coupling. According to the Oguchi criterion [30], a Néel temperature of $T_{\mathrm{N}} = 0.25$ K and the intra-chain coupling constant of $|J/k_{\mathrm{B}}| = 3$ K correspond to a ratio of inter-chain to intra-chain coupling less than $\sim 10^{-4}$ for $S = 5/2$ spin chains. Thus we may conclude from the low-temperature susceptibility data that BMZ is a very good realization of an antiferromagnetic $S = 5/2$ Heisenberg spin-chain system.

Unlike the BMZ system discussed above, the magnetic susceptibilities for BMM and BMC are both governed by large paramagnetic contributions. This is not surprising in view of the structural properties of these systems, yielding—as the only difference—magnetically isolated $MnCl_4$ (BMM) or $CoCl_4$ tetrahedra (BMC), which are replaced by non-magnetic $ZnCl_4$ tetrahedra in BMZ. The structural parameters, like bond distances and bond angles within the magnetic spin chains of BMM, BMC and BMZ, are almost identical (see tables 2 and 3). Given the similar structural parameters of these compounds, it is possible to analyse the magnetic properties of BMM and BMC in more detail.

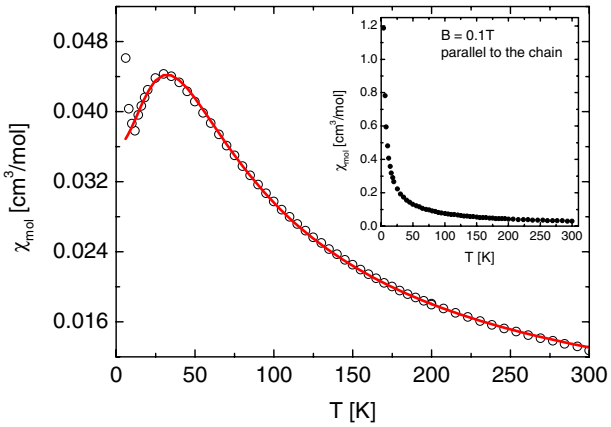

Figure 6. Molar magnetic susceptibility χ_{mol} of 3b·2$MnCl_2$ (BMM) in a field of $B = 0.1$ T applied parallel to the c-axis after subtracting the paramagnetic contribution due to magnetically isolated Mn–Cl tetrahedra. The solid line is a fit to the experimental data based on a model of an antiferromagnetic Heisenberg spin chain. Inset: the raw data before subtraction.

In the compound BMM we treat the magnetic contribution of the $MnCl_4$ tetrahedra, which corresponds to 50% of the total amount of Mn^{2+} ions, as free spins with $S = 5/2$. By subtracting the corresponding Curie susceptibility from the raw data, we obtain the susceptibility originating from the chains of coupled MnO_6 octahedra (figure 6). The resulting $\chi_{mol}(T)$ is very similar to the data for BMZ shown in figure 5. Employing the same fitting procedure as for the latter system yields, within the error margins, the same antiferromagnetic intra-chain coupling constant $J/k_B = -(3.0 \pm 0.15)$ K for BMM.

For BMC, the analysis of the magnetic data is hampered by the presence of the Co ions. Firstly, depending on its coordination environment, the crystal field splitting of the Co^{2+} ions can give rise to a temperature-dependent contribution to the susceptibility. Secondly, site-exchange between Mn and Co ions may have occurred within the uncertainty of ∼10% implied in our structural analysis. Assuming that at least 90% of the tetrahedral sites are occupied by the Co^{2+} ions (a value consistent with X-ray diffraction experiments), whereas the Mn^{2+} ions are predominantly in an octahedral coordination, the room-temperature susceptibility would correspond to an effective magnetic moment for the Co^{2+} ions of $\mu_{eff} \sim 4.6\ \mu_B$. Such a value is compatible with Co^{2+} in a tetrahedral coordination [31]. Under these conditions the effective moment of the Co^{2+} ions is nearly temperature independent, which enables us to perform an analysis similar to that employed for BMM. As a result, we find that in BMC the octahedrally coordinated Mn^{2+} ions forming the spin chains are also coupled antiferromagnetically with $J/k_B = (-3.0 \pm 0.3)$ K, whereas the $CoCl_4$ tetrahedra are magnetically isolated.

5. Summary

The three isomorphous compounds 3b·$MnCl_2$·MCl_2 with M = Mn^{2+}, Co^{2+} and Zn^{2+} exhibit three different cation sites, two in octahedral and one in tetrahedral coordination, in the ratio 1:1:2. Isomorphic replacement takes place on the tetrahedral site only (BMZ) or at least predominantly (BMC), leaving the octahedral chains occupied by manganese in all three compounds. Thus the common feature is the chain of carboxylate-bridged Mn^{2+} ions ($S = 5/2$), which are coupled antiferromagnetically. The second metal in the isolated MCl_4 tetrahedra influences the magnetic properties considerably, depending on spin state (Mn 5/2,

Co 3/2, Zn 0), as the paramagnetic moment of the isolated spins at low temperatures is much larger than the contribution of the coupled spins in the chain.

Thus, the Mn–Zn compound (BMZ) is the only one where the magnetic properties of the chains are seen in pure form. In BMM and BMC, on the other hand, the chain contribution could be modelled after subtracting the paramagnetic contribution of the isolated spins in the $MnCl_4$ tetrahedra.

An essential point of these magnetic model calculations is the occupation of metal sites. A certain number of $S < 5/2$ ions in the octahedral sites would interrupt the magnetic interaction and, vice versa, changing the size and number of free spins in the tetrahedral sites influences the paramagnetic contribution. A possible mixing of different spin states on both lattice sites cannot be modelled from the magnetic data alone, but needs the knowledge of chemical composition.

For BMZ there is a clear chemical preference for MnO_6 octahedra and $ZnCl_4$ tetrahedra. The quantum mechanical calculations show that it is energetically very unfavourable to incorporate Zn into the octahedral sites in BMZ. This result is confirmed by X-ray diffraction, which is able to deliver significant occupation factors in the Mn–Zn case. Moreover, the results of Heisenberg chain modelling in BMM and BMZ show the equivalence of these chains in both compounds. Thus the quantitative consistence of all these results demonstrates the capability of the DFT method.

For BMC, on the other hand, no pronounced chemical preferences exist. X-ray diffraction can only narrow the extent of disorder down to less than 20%. This limit is further reduced by the results of magnetic measurements, which are compatible only with an amount significantly less than 10% Co in the magnetically coupled Mn chain.

In summary, the magnetic properties of all three compounds BMZ, BMM and BMC are well described by independent Heisenberg spin chains formed by octahedrally coordinated Mn^{2+} ions with $S = 5/2$. The weak antiferromagnetic intra-chain coupling of $J/k_B \sim -3.0$ K for all three compounds is provided by the π-electron system of the carboxylate groups at the ends of the betaine molecules. The metal ions on the tetrahedral positions are magnetically isolated and do not influence the magnetic properties of the spin chains. This explains the similarity of the magnetic parameters of BMC, BMM and BMZ and is consistent with their structural properties.

Acknowledgments

Financial support of the Forschergruppe 412 ‘Spin- und Ladungskorrelationen in niedrigdimensionalen Festkörpern’ from the Deutsche Forschungsgemeinschaft (DFG) is gratefully acknowledged.

References

[1] Albers J, Klöpperpieper A, Rother H J and Ehses K H 1982 Antiferroelectricity in betaine phosphate *Phys. Status Solidi* a **74** 553–7

[2] Unruh H-G, Hero F and Dvorak V 1989 On the incomplete devil’s staircase of betaine calcium chloride dihydrate *Solid State Commun.* **70** 403–8

[3] Chaves M R, Almeida A, Tolédano J C, Schneck J, Kiat J M, Schwarz W, Ribeiro J L, Klöpperpieper A, Albers J and Müser H E 1993 Effect of electric fields on modulated structure of deuterated betaine calcium chloride dihydrate *Phys. Rev.* B **48** 13318–25

[4] Ramos Silva M, Paixão J A, Matos Beja A, Alte da Veiga L and Martín-Gil J 2001 Crystal structure of tetrakis (μ-betaine-O,O’) dichloro-dicopper(II) dichloride tetrahydrate *J. Chem. Crystallogr.* **31** 167–71

[5] Chow M-Y, Zhou Z-Y and Mak T C W 1992 A linear polymeric copper(II) complex bridged simultaneously by azido, nitrato, and betaine ligands. Crystal structure of catena-[bis(μ-(1,1)-azido)bis(μ-nitrato-

O,O')bis-((μ-trimethylammonio)acetato-O,O')dicopper(II)], $[Cu_2(N_3)_2(NO_3)_2(Me_3NCH_2CO_2)_2]_n$ *Inorg. Chem.* **31** 4900–2

[6] Chen X-M and Mak Th C W 1991 A linear polymeric manganese(II) complex bridged by skew–skew bridging carboxylato groups. Crystal structure of *catena*-tris(betaine)manganese(II) tetrachloromanganate(II), $[Mn(Me_3NCH_2COO)_3]_n \cdot n\ MnCl_4$ *Inorg. Chim. Acta* **189** 3–5

[7] Schreuer J and Haussühl S 1993 Crystal structure of catena-tri-μ-trimethylammonium acetatomanganese tetrachloromanganate $(((CH_3)_3NCH_2COO)_3Mn)MnCl_4$ *Z. Kristallogr.* **205** 309–10

[8] Schreuer J and Haussühl S 1993 Crystal structure of catena-(trimethylammoniumacetato) tetrachloro-aqua-dimanganese, $((CH_3)_3NCH_2COO)Cl_4(H_2O)Mn_2$ *Z. Kristallogr.* **205** 313–5

[9] Tong Y-X, Chen X-M and Ng S W 1997 Synthesis and crystal structures of two polymeric cadmium(II) complexes containing skew-skew carboxylato-bridges *Polyhedron* **16** 3363–9

[10] Wiehl L, Schreuer J and Haussühl E 2006 Crystal structures of *catena*-(tris(μ-betaine-O,O')manganese(II)) tetrachlorozincate and *catena*-(tris(μ-betaine-O, O')manganese(II)) tetrachloro-cobaltate, $[\{(CH_3)_3NCH_2COO\}_3Mn][MCl_4]$ (M = Zn, Co) *Z. Kristallogr. NCS* **221** 77–9

[11] Kahn O 1993 *Molecular Magnetism* (New York: VCH)

[12] Hohenberg P and Kohn W 1964 Inhomogeneous electron gas *Phys. Rev.* **136** B864–71

[13] Perdew J P, Chevary J A, Vosko S H, Jackson K A, Pederson M R, Singh D J and Fiolhais C 1992 Atoms, molecules, solids and surfaces: applications of the generalized gradient approximation for exchange and correlation *Phys. Rev.* B **46** 6671–87

[14] Leung T C, Chan C T and Harmon B N 1991 Ground-state properties of Fe, Co, Ni and their monoxides: results of the generalized gradient approximation *Phys. Rev.* B **44** 2923–7

[15] Hammer B, Jacobsen K W and Norskov J K 1993 Role of nonlocal exchange–correlation in activated adsorption *Phys. Rev. Lett.* **70** 3971–4

[16] Goniakowski J, Holender J M, Kantorovich L N, Gillan M J and White J A 1996 Influence of gradient corrections on the bulk and surface properties of TiO_2 and SnO_2 *Phys. Rev.* B **53** 957–60

[17] Hamann D R 1996 Generalized gradient theory for silica phase transitions *Phys. Rev. Lett.* **76** 660–3

[18] Bachelet G B, Hamann D R and Schlüter M 1982 Pseudopotentials that work: from H to Pu *Phys. Rev.* B **26** 4199–228

[19] Kleinman L and Bylander D M 1982 Efficacious form for model pseudopotentials *Phys. Rev. Lett.* **48** 1425–8

[20] Vanderbilt D 1990 Soft self-consistent pseudopotentials in a generalized eigenvalue formalism *Phys. Rev.* B **41** 7892–5

[21] Kresse G and Hafner J 1994 Norm-conserving and ultrasoft pseudopotentials for first-row and transition elements *J. Phys.: Condens. Matter* **6** 8245–57

[22] Payne M C, Teter M P, Allan D C, Arias T A and Johannopoulos J D 1992 Iterative minimisation techniques for ab initio total energy calculations—molecular dynamics and conjugate gradients *Rev. Mod. Phys.* **64** 1045–97

[23] Milman V, Winkler B, White J A, Pickard C J, Payne M C, Akhmatskaya E V and Nobes R H 2000 Electronic structure, properties, and phase stabilities of inorganic crystals: a pseudopotential plane-wave study *Int. J. Quantum Chem.* **77** 895–910

[24] Segall M D, Lindan P J D, Probert M J, Pickard C J, Hasnip P J, Clark S J and Payne M C 2002 First-principles simulation: ideas, illustrations and the CASTEP code *J. Phys.: Condens. Matter* **14** 2717–44

[25] Wells A F 1984 *Structural Inorganic Chemistry* 5th edn (Oxford: University Press)

[26] Milman V and Winkler B 2001 Prediction of hydrogen positions in complex structures *Z. Kristallogr.* **216** 99–104

[27] Shannon R D 1976 Revised effective ionic radii and systematic studies of interatomic distances in halides and chalcogenides *Acta Crystallogr.* A **32** 751–67

[28] Hiller W, Strähle J, Datz A, Hanack M, Hartfield W E and Gütlich P 1984 *J. Am. Chem. Soc.* **106** 329

[29] Smart J S 1966 *Effective Field Theories of Magnetism* (Philadelphia, PA: Saunders)

[30] Oguchi T 1964 *Phys. Rev.* **133** A1098

[31] Lueken H 1999 *Magnetochemie* (Stuttgart/Leipzig: B T Teubner Verlag)